ROYAL SOCIETY OF CHEMISTRY

PAPER

Check for updates

Is a small singlet–triplet energy gap a guarantee of TADF performance in MR-TADF compounds? Impact of the triplet manifold energy splitting†

Rasa Keruckiene, [iD] [a] Aliaksei A. Vaitusionak, [b] Maksim I. Hulnik, [b] Ivan A. Berezianko, [b] Dalius Gudeika, [a] Simas Macionis, [a] Malek Mahmoudi, [a] Dmytro Volyniuk, [iD] [a] Danillo Valverde, [iD] [c] Yoann Olivier, [iD] *[c] Kai Lin Woon, [iD] [d] Sergei V. Kostjuk, [iD] [be] Sebastian Reineke, [iD] [f] Juozas V. Grazulevicius [iD] *[a] and Gjergji Sini*[g]

Aiming at obtaining pure-color emitters for organic light-emitting diodes (OLEDs), we designed and synthesized a new organic boron-containing indolocarbazole derivative as a candidate for multiple resonance-induced thermally activated delayed fluorescence (MR-TADF) emitters. The efficiency of the targeted MR and TADF characteristics are analyzed by steady-state and time-resolved spectroscopy at different temperatures, and by different theoretical methods. The molecule exhibits green-yellow photoluminescence and electroluminescence with a full-width at half-maximum (FWHM) of 20 nm and 23 nm for thin films observed from photoluminescence (PL) and electroluminescence spectra. The PL intensity increases by up to 100% for the degassed sonicated toluene solutions; however, no TADF behavior is observed. The increase in PL is predominantly due to the decrease of the singlet quenching by the dissolved oxygen and by the remaining microaggregates in solution, as opposed to the frequently reported quenching of triplet excitons by oxygen. The absence of TADF behavior in toluene solution is attributed to very small spin–orbit coupling between S_1 and T_1 (0.02 cm^{-1}) and a large T_1–T_2 gap that inhibits the $T_1 \rightarrow T_2$ upconversion of triplets which likely results in a very low rate of intersystem crossing as compared to the radiative decay rate. However, a weak TADF is observed in guest–host mixtures, *e.g.*, in thin films made with mCP, DPEPO, and Zeonex hosts. This is attributed to the reduced T_1–T_2 gap, resulting from the conformational distortions of the emitter in the guest–host systems. Even with 100% photoluminescence quantum yields of the toluene solution, the efficiency of the first prototypical OLEDs is limited. Different sources for the low device external quantum efficiency are discussed. Ultimately, our structure–property analysis suggests a design rule allowing tuning of the T_1–T_2 gap for more efficient TADF.

[a] *Department of Polymer Chemistry and Technology, Kaunas University of Technology, K. Barsausko st. 59, LT-50254, Kaunas, Lithuania. E-mail: juozas.grazulevicius@ktu.lt*

[b] *Research Institute for Physical Chemical Problems of the Belarusian State University, 14, Leningradskaya st 220030 Minsk, Belarus*

[c] *Laboratory for Computational Modeling of Functional Materials, Namur Institute of Structured Matter, University of Namur, Rue de Bruxelles, 61, B-5000 Namur, Belgium*

[d] *Low Dimensional Material Research Centre, Department of Physics, University Malaya, Kuala Lumpur, Malaysia*

[e] *Department of Chemistry, Belarusian State University, Leningradskaya st. 14, 220006, Minsk, Belarus*

[f] *Dresden Integrated Center for Applied Physics and Photonic Materials (IAPP), Technische Universität Dresden, Dresden 01062, Germany*

[g] *Laboratoire de Physicochimie des Polymères et des Interfaces, EA 2528, CY Cergy Paris Université, 5 mail Gay-Lussac, 95031 Cergy-Pontoise Cedex, France*

† Electronic supplementary information (ESI) available. See DOI: **https://doi.org/10.1039/d3tc04397e**

1. Introduction

The field of thermally activated delayed fluorescence (TADF) has witnessed remarkable advancements, thanks to the synthesis of various TADF molecules incorporating diverse electron and donor moieties within a donor–acceptor (D–A) architecture.[1–11] Achieving high efficiency with these molecules necessitates an extremely low exchange energy, leading to a near-zero energy splitting between the first singlet- and triplet excited states (ΔE_{ST}) of less than 0.03 eV.[12–14] This is one of the crucial parameters that facilitate the induction of reverse intersystem crossing (RISC), a process made possible through the vibronic coupling with torsion mode around the D–A bond.[15,16]

However, the flexibility inherent in the D–A bond, while essential, gives rise to a challenge. This architectural characteristic introduces conformational disorder, significantly

3450 | *J. Mater. Chem. C,* 2024, **12**, 3450–3464

This journal is © The Royal Society of Chemistry 2024

broadening the emission spectra and compromising the desired color purity—a stringent requirement for display applications, and efforts to circumvent the shortcomings were met with limited success.[17–19] The discovery of multi-resonance TADF (MR-TADF) by Hatakeyama et al. has ushered in a paradigm shift in TADF design.[20] By employing a rigid polycyclic aromatic framework, MR-TADF exhibits a narrow emission bandwidth coupled with high oscillator strength compared to conventional D–A TADF architecture, together with a small ΔE_{ST}. The small ΔE_{ST} is achieved by effectively spatially separating the highest occupied molecular orbital (HOMO) and lowest unoccupied molecular orbital (LUMO) distributions on adjacent neighboring atomic sites thanks to opposite resonant effects while maintaining sufficient overlap to guarantee a high oscillator strength.[21–24]

First MR-TADF materials (DABNA-1 and DABNA-2) were reported in 2016 by Hatakeyama et al.[25] These compounds contain a central boron atom and para-disposed nitrogen atoms that achieve the desired alternating pattern of the electron density distribution. Devices fabricated from DABNA-1 and DABNA-2 showed a maximum EQE of 13.5% and 20.2% with CIE coordinates of (0.13, 0.09) and (0.12, 0.13), respectively. The MR based design approach provided sharp EL spectra with FWHMs of 30 and 28 nm for DABNA-1 and DABNA-2, respectively. However, the low rate of RISC resulted in a severe efficiency roll-off. The MR effect in DABNA-1 was further enhanced by changing its structure either by attaching nitrogen phenyl rings with t-butyl groups[26] or by further addition of tert-butyl carbazole[27] and di(tert-butylphenyl)amine[28] moieties at the para-position of the boron atom. Thus, all TADF properties of the DABNA-1 derivative, TBN-TPA, were significantly improved, resulting in a high EQE of 32.1% and FWHM of 27 nm, except for the 15 nm red-shift of the EL spectrum.[27] By fusing two DABNA-1 molecules, ν-DABNA was designed, and it was reported to exhibit a quite sharp EL peak (FWHM = 18 nm) at 469 nm and a high EQE of 34.4%.[29] Duan et al.[30] developed a new strategy of extending the conjugation of the DABNA-1 core by simply replacing the diphenylamine unit with tert-butylcarbazole (BCz-BN). Thus, the first series of green MR-TADF emitters with EQEs of up to 22.4% and FWHM of up to 29 nm was reported. By introduction of four extra tert-butylphenyl groups on the carbazole moieties Wang et al.[31] expanded the conjugation skeleton and therefore reported highly efficient (EQE of 25.5%), stable (high EQE of 20.1% was maintained at a practical high luminance of 1000 cd m^{-2}), narrowband (FWHM of 33 nm) and pure green emitters with CIE coordinates of (0.20, 0.65). Subsequently, a large number of studies have been carried out, aiming to extend the conjugation of the DABNA-1 core and to improve device performance, which resulted in synthesis of blue,[32,33] green,[30,32,34–37] yellow[34,36] and orange-red[35] MR-TADF emitters by introducing into the DABNA-1 structure a variety of electron-deficient and electron-rich groups. The main tendency observed is that electron-deficient moieties in DABNA (e.g., CN and F) lead to a bathochromic shift of its emission spectra: a high performance OLED device with an outstanding EQE as high as 33.7% and orange-red luminescence was fabricated by introducing cyano substituents.[36]

Despite the large number of efforts oriented towards the design and synthesis of MR-TADF emitters, clear design rules for new compounds are still missing but urgently needed. While the detailed RISC mechanism is not yet elucidated in MR-TADF, a small ΔE_{ST} between S_1 and T_1 is often seen as a prerequisite for TADF to take place. If the direct RISC occurs from the first triplet excited state (T_1) to the first singlet excited state (S_1) as proposed by Lin et al.,[38] a decrease in ΔE_{ST} is expected to lower the activation energy for RISC to take place. Pershin et al.,[39] through computational modeling, have demonstrated that ΔE_{ST} can be reduced by increasing the π-conjugation of MR-TADF and thus by increasing the excited state electronic density delocalization. However, several studies have shown that S_1 and T_1 states in these MR-TADF compounds are of the same nature, which, by virtue of El Sayed's rule, limits a direct transition of triplet excitons from T_1 to S_1. In this context, it has been shown[40–44] that internal upconversion from T_1 to some higher but low-lying triplet states from which RISC takes place is an alternative path for the TADF mechanism to be efficient. Accordingly, the efficiency of the TADF contribution to the triplet harvesting of the MR-TADF compounds in solution depends on this T_1–T_n energy gap, and the $S_1(S_n)$–T_n spin–orbit couplings (SOC). Designing MR-TADF compounds by solely targeting the smallest $\Delta E_{S_1-T_1}$ may then be insufficient, thus rendering important the presence of a dense manifold of triplet excited states up to the S_1 energy.

Here, we address focus on both small $\Delta E_{S_1T_1}$ and small T_1–T_n ($n > 1$) energy splitting. To this aim, we have synthesized a boron-based indolocarbazole derivative, an elongated MR-TADF molecule. This compound has a significantly reduced $\Delta E_{S_1T_1}$ but a large T_1–T_2 energy splitting, resulting in inefficient triplet harvesting. The analysis of the reasons for this large T_1–T_2 energy splitting allowed us to suggest a new design rule helping to avoid the problem.

2. Results and discussion

2.1 Synthesis

Boron-based compound **DG7** was successfully synthesized using a three step synthetic route starting from commercially available 5,11-dihydro-indolo[2,3-b]carbazole, as presented in Scheme 1. In the first two steps, monosubstituted indolocarbazole (**dg7-2**) was obtained via an Ullmann amination reaction with iodobenzene followed by nucleophilic substitution catalyzed by potassium tert-butoxide (t-BuOK) affording **dg7-1**. The final target molecule **DG7** was synthesized by a one-pot reaction via a lithium–halogen exchange reaction with n-butyllithium, electrophilic trapping with boron tribromide, and high-temperature tandem electrophilic arene borylation in the presence of diisopropylethylamine. The structure of the target compound was confirmed by X-ray single crystal analysis and ^{1}H NMR spectroscopy (see Experimental in the ESI†).

Thermal, electrochemical, charge-injecting and charge-transporting properties. The thermal stability and morphological properties of the synthesized compound **DG7** were investigated by
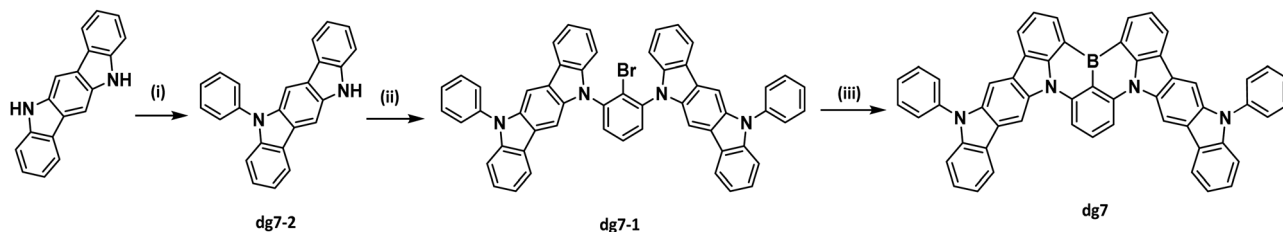
Scheme 1 Synthetic route to boron-based compound **DG7**: (i) iodobenzene, CuI, 1,10-phenanthroline, K_2CO_3, 18-crown-6, DMF, 20 h at 140 °C, (ii) 1-bromo-2,6-difluorobenzene, *t*-BuOK, DMF, 48 h at 100 °C, (iii) *n*-BuLi, *tert*-butylbenzene, 4 h at r.t.; BBr_3, 12 h at r.t., *N,N*-diisopropylethylamine, 24 h at 170 °C.
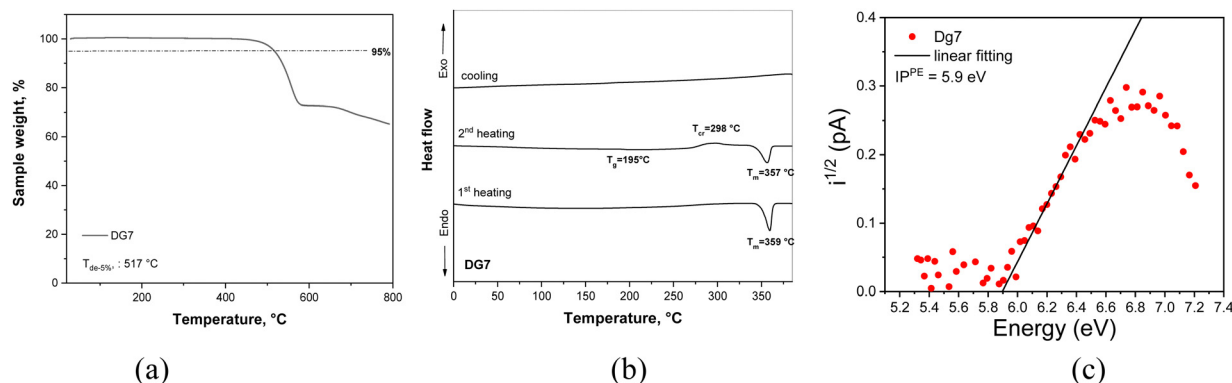

Fig. 1 TGA (a), DSC (b) and photoelectron emission (c) curves of compound **DG7**.

thermogravimetric analysis (TGA) and differential scanning calorimetry (DSC) under a nitrogen atmosphere as shown in Fig. 1. It was found that **DG7** demonstrated very high thermal stability and the 5% weight-loss temperature ($T_{d-5\%}$, °C) of the compound was about 517 °C (Fig. 1a) confirming its excellent thermal stability and it can be considered as a thermally stable material appropriate for light emitting vacuum deposited devices.[45] DSC measurements revealed that compound **DG7** was isolated as a crystalline solid which was proved by its well-defined melting points (T_m, °C). During the second heating scan between −20 °C and 390 °C with a heating rate of 10 °C min^{-1}, a glass transition temperature of 195 °C, a crystallization temperature of 298 °C and a melting point of 357 °C were recorded (Fig. 1b and Table 1).

The electrochemical properties of **DG7** were investigated by cyclic voltammetry (CV). The voltammograms are presented in Fig. S1a (ESI†), and the derived data are presented in Table 1. **DG7** showed quasi-reversible oxidation and reduction in the potential range from −1.8 to 1.8 V. By utilizing the potential oxidation ($E_{ox\,vs.\,Fc/Fc^+}$) of **DG7**, the quite high ionization potential value (IP_{CV}) of 5.58 eV of the sample implies a not too strong electron donating characteristic of the sample. Nevertheless, the determined electron affinity suggests a well-balanced oxidation–reduction process upon electrical induction of the sample. By utilizing the potential reduction ($E_{red\,vs.\,Fc/Fc^+}$) of **DG7**, we obtained an electron affinity (EA_{CV}) value of 3.63 eV (Table 1).

To investigate the charge-injecting capabilities of **DG7**, we conducted photoelectron emission (PE) measurements in an air environment. Using data from solid films of **DG7**, an

Table 1 Thermal, electrochemical, photoelectrical, hole-transporting and photophysical parameters of **DG7**

Property	Sample	DG7
T_m,[a] °C	Powder	357
T_g,[a] °C		195
T_{cr},[a] °C		298
$T_{de-5\%}$,[b] °C		517
$E_{ox\,vs.\,Fc/Fc^+}$, V	DCM solution with TBAPF$_6$	0.75
$E_{red\,vs.\,Fc/Fc^+}$, V		−1.47
IP_{CV}, eV		5.85
EA_{CV}, eV		3.63
IP_{PE}, eV	Film	5.9
EA_{PE}, eV		3.7
μ_h,[c] cm^2 (V s)$^{-1}$		3.4×10^{-6}

[a] Taken from the 2nd heating scan of DSC measurement. [b] 5% weight loss, taken from TGA measurement. [c] Obtained by CELIV measurements at an electric field of 2×10^4 V cm^{-1}.

ionization potential (IP_{PE}) of 5.9 eV and an electron affinity (EA_{PE}) of 3.7 eV were obtained (Table 1) based on PE and absorption spectra. The energy levels of **DG7** from CV and PE measurements agree well. The charge-transporting ability of **DG7** was investigated using time-of-flight (TOF) and charge extraction by linearly increasing voltage (CELIV) methods (Fig. S1b–d, ESI†). The vacuum-deposited films of **DG7** exhibited hole-transporting properties with a hole mobility (μ_h) of 3.4×10^{-6} cm^2 (V s)$^{-1}$ under a low electric field of 2×10^4 V cm^{-1} (Table 1). The electroluminescent properties of **DG7** were tested using charge-injecting and charge-transporting data (refer to the last section).

3452 | *J. Mater. Chem. C*, 2024, **12**, 3450–3464

This journal is © The Royal Society of Chemistry 2024

2.2 Geometrical and electronic structure characteristics

The ground-state optimized geometry of **DG7** and some selected molecular orbital (MO) pictures are presented in Fig. 2. The ground-state molecular structure is almost planar, yet the steric hindrance between the closely lying peripheral benzene rings induces some helicoidal-wise deformation of the molecular plane, with a pitch of roughly 19° between their plans, see Fig. 2a. The HOMO and LUMO are both delocalized on the central part of the molecule including contribution from the carbazole inner moieties of the indolocarbazole fragments (Fig. 2b), whereas HOMO−1 and LUMO+1 are localized on the indolocarbazole fragments with no contribution from the boron atom.

For the sake of better understanding the excited state properties of **DG7**, we computed vertical excitation energies using the spin-component scaling second-order approximate coupled-cluster (SCS-CC2) together with the cc-pVDZ basis set. This level of theory has been shown to accurately describe the excited states of MR-TADF compounds.[46] Our results indicate that the S_1 state is predominantly described by a HOMO to LUMO transition (80% weight) with a high oscillator strength (f = 0.701). A similar electronic nature is obtained for the T_1 state, as can be seen in the difference-density plot (Fig. 3c). Because of the similar nature of S_1 and T_1 as testified by their nearly identical electronic density distributions, the SOC value is quite small (0.02 cm^{-1}), in line with the El-Sayed rule. Interestingly, both S_1 and T_1 states exhibit a short-range CT (SRCT) character, which is an intrinsic feature of MR-TADF compounds. The singlet–triplet energy gap between the S_1 and T_1 states is predicted to be 0.09 eV, in good agreement with the experimental data (0.19 eV, *vide infra*). The second singlet state lies 0.48 eV above the S_1 states and has almost null oscillator strength (f = 0.001) (see Table S1, ESI†). The T_2 and T_3 triplet states can be potentially intermediate states for the RISC, since they are nearly degenerate and positioned merely 0.22 eV above the S_1 state (see Table S1, ESI†). Additionally, the SOC value between S_1 and T_3, and between S_2 and T_2 are considerably higher than that between S_1 and T_1 (0.50 cm^{-1} for $S_2 \to T_2$, and 0.44 cm^{-1} for $S_1 \to T_3$) because of the very different electronic-density localization of both T_2 and T_3 states in comparison to S_1.

Excited-state geometry optimizations of the first lowest singlet and triplet states were carried out at the TD-PBE0/6-31G(d,p) level. Both optimized structures resemble the ground-state minimum structure, as can be seen by superimposing the ground- and excited-state structures (see Fig. S2, ESI†). Due to the very similar excited-state structures for both S_1 and T_1 the adiabatic ΔE_{ST} is close to the one obtained from vertical excitation from the ground state (see Table S2, ESI†).

2.3 Photophysical properties in toluene solution and neat film

The photophysical properties of dilute toluene, tetrahydrofuran (THF) (concentration of 10^{-5} M) and also neat films of the target compound were studied. UV-vis absorption and steady state PL spectra of the compound are presented in Fig. 3 and the selected spectral data are summarized in Table 1.

The absorption spectrum of the THF solution of the compound showed four bands with maxima at 522, 387, 321, and 305 nm, while the solid sample UV spectrum exhibited maxima at 532, 392, 325, and 309 nm which proves a similar absorption profile with a small redshift for neat film in comparison to solution of the compound. As depicted in Fig. 3a, compound **DG7** exhibits an intense and sharp absorption band around 530 nm. The longer maximum wavelength as compared to other MR-TADF compounds like DABNA-1 is due to the more extended π-conjugation *via* the fused indolocarbazole moieties, whereas the sharpness of the absorption band is due to the rigid molecular skeleton hosting the multi resonance-induced charge transfer transition.[47]

Emission spectra of the **DG7** emitter excited at 350 nm show a small, red-shifted maximum upon increasing the solvent polarities from toluene to THF, confirming the SRCT nature of the S_1 state (Fig. 3b).[48] The green-yellow emission of the solutions of **DG7** is still rare and was reported for MR-TADF only once before.[49,50] These emission characteristics make **DG7** a perfect candidate for hyperfluorescent based OLEDs. The Stokes shifts of diluted toluene solution and neat film PL spectra of **DG7** are only 21 nm (0.09 eV) and 34 nm (0.14 eV) with respect to their absorption maxima, indicating that its molecular relaxation is highly restricted. This very small Stokes shift is similar to the ones observed in other† MR-TADF
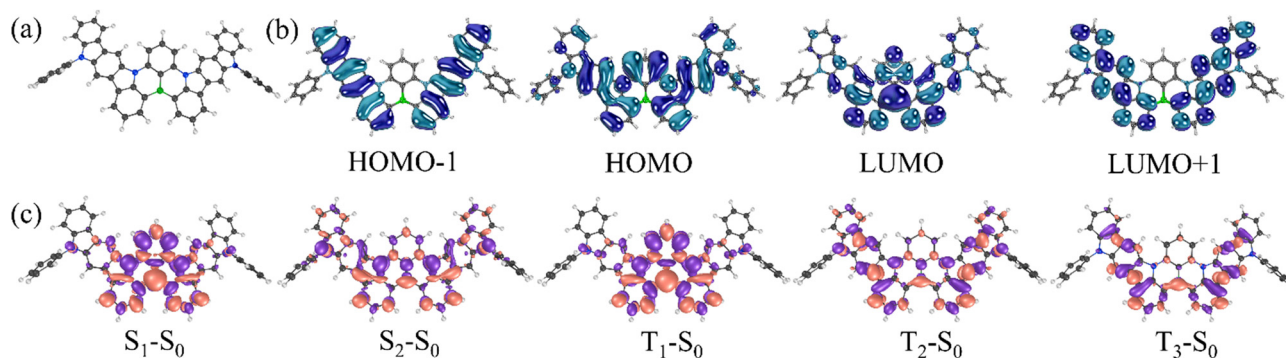

Fig. 2 (a) Ground-state molecular structure of **DG7** optimized at the PBE0/6-31G(d,p) level. (b) Shape of some selected MOs of **DG7**, and (c) the difference density plot between the ground-state and the selected excited state (singlet or triplet).
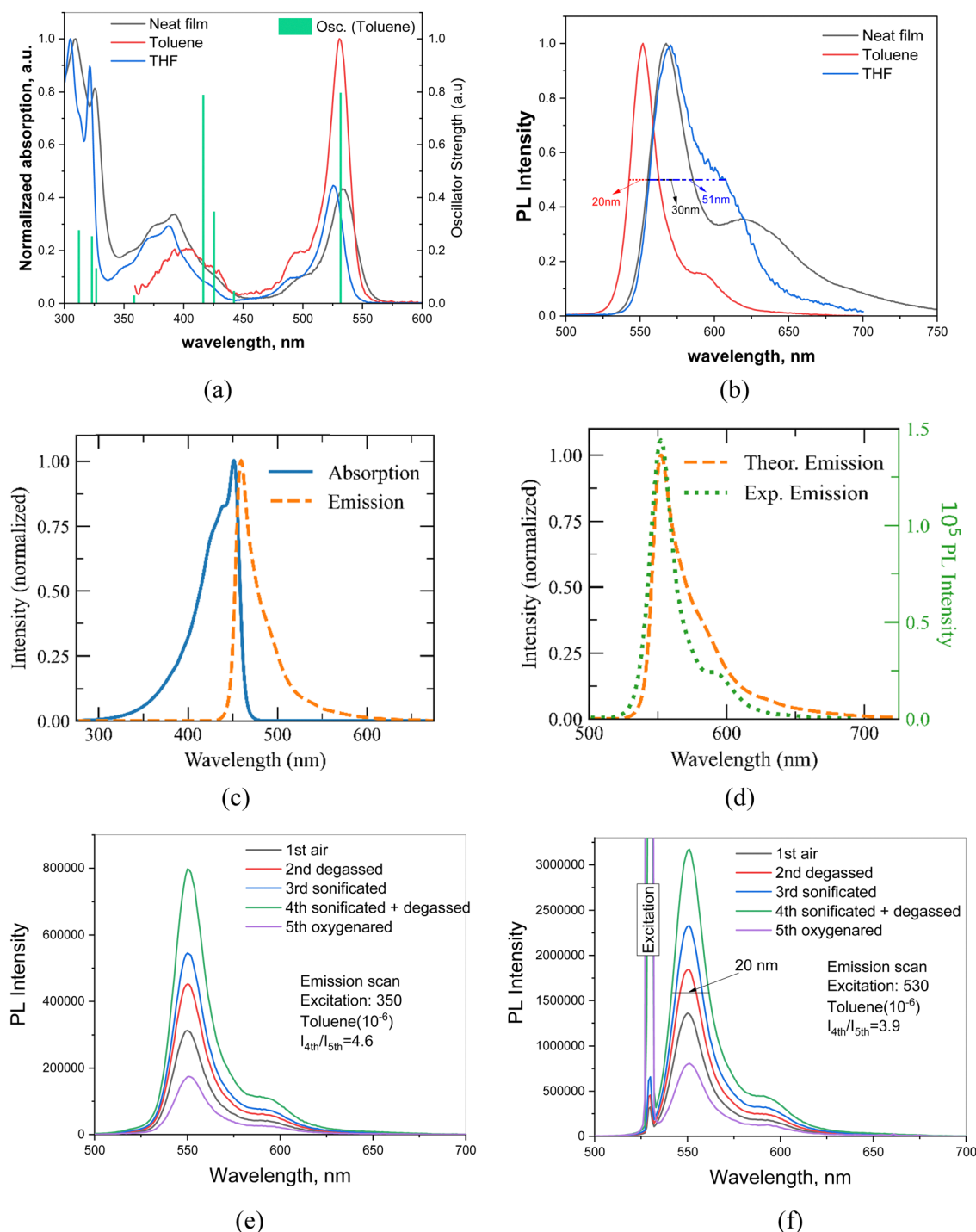
Fig. 3 (a) UV-vis and (b) photoluminescence spectra of toluene or THF solutions and neat film of **DG7**. (a) The green-vertical bars (oscillator strengths) correspond to the theoretical absorption spectrum calculated at the hole–hole Tamm–Dancoff approximated density functional theory (hh-tda) using the B3LYP functional with the def2-svp basis set.[53] The theoretical excited state energies are blue-shifted by 0.48 eV in order to fit the energy of S_1 with the maximum of the experimental low-energy band. (c) and (d) Theoretical absorption and emission spectra obtained at the SCS-CC2/cc-pVDZ level of theory. The simulated spectrum in panel (d) is redshifted by 93 nm to fit with the experimental peak. (d) PL decay curve of the mCP-doped film of **DG7**. (e) and (f) Emission scans of **DG7** in toluene (10^{-6}) from 500 to 700 nm (e) under excitation at 350 nm and (f) under excitation at 530 nm, for 5 different conditions of solution.

materials[51,52] and finds support from the theoretical calculations (*vide supra*).

The vibronically resolved absorption and emission spectra of **DG7** were emulated (Fig. 3c) within the displaced undistorted harmonic oscillator model in conjunction with the thermal vibration correlation functional formalism, as implemented in MOMAP/2022A (see the ESI† for further computational details) within the Franck–Condon approximation. Absorption and

3454 | *J. Mater. Chem. C*, 2024, **12**, 3450–3464

This journal is © The Royal Society of Chemistry 2024

emission theoretical spectra are shown in Fig. 3a, c and d. Fig. 3a indicates that the lowest-energy absorption band is due to only the 1st excited state (S_1), whereas the band peaking around 400 nm includes contributions from the closely lying S_2–S_4 excited states. A small FWHM value of 29.4 nm is obtained at the theoretical level, as compared to the experimental value of 17.6 nm in toluene solution (Fig. 3c and d). This small broadening is essentially modulated by a low vibrational normal mode (frequency of 25 cm^{-1} and Huang–Rhys factor of 2.3) characterized by a collective twisting motion of the hydrogen atoms of the phenyl groups (see Fig. S3, ESI†). In Fig. 3d, the simulated emission spectrum is redshifted in relation to the experimental data in toluene in order to match the main experimental peak. The experimental low energy weak emission peak is well reproduced by the theoretical calculations, indicating contribution from the 0–1 vibrational replica in addition to the 0–0 one. According to our theoretical results, the Stokes shift, computed from the absorption and emission peaks, is 7 nm (0.05 eV), confirming the small reorganization energy of the S_1 state (see Fig. S4, ESI†).

It is worth noting that possible contribution from the excimer emission in toluene solutions has been previously reported falling in the same region as the theoretical 0–1 vibrational replica of the emission band.[54] Interestingly, the sonication of the toluene solutions at different concentrations of **DG7** indicates an important increase in the emission intensity (Fig. 3e and f), witnessing the presence of microaggregates and the corresponding aggregation caused quenching (ACQ) in solution. Nevertheless, when varying the concentration from 10^{-4}–10^{-6} mol L^{-1}, the intensity ratio between the main and the weak-energy peaks remains unchanged ($I_M/I_W = 7$, Fig. S5, ESI†), suggesting the absence of excimer emission independently of the presence of microaggregates in toluene solution. This conclusion seems to find support from the time-resolved emission spectra (TRES) measurements: the PL spectra of toluene solutions of **DG7** are practically the same at different excitation wavelengths and different delay times after excitation (Fig. 4a and Fig. S6 and S7, ESI†), thus excluding the presence of different emission species in solution. Upon photoexcitation,
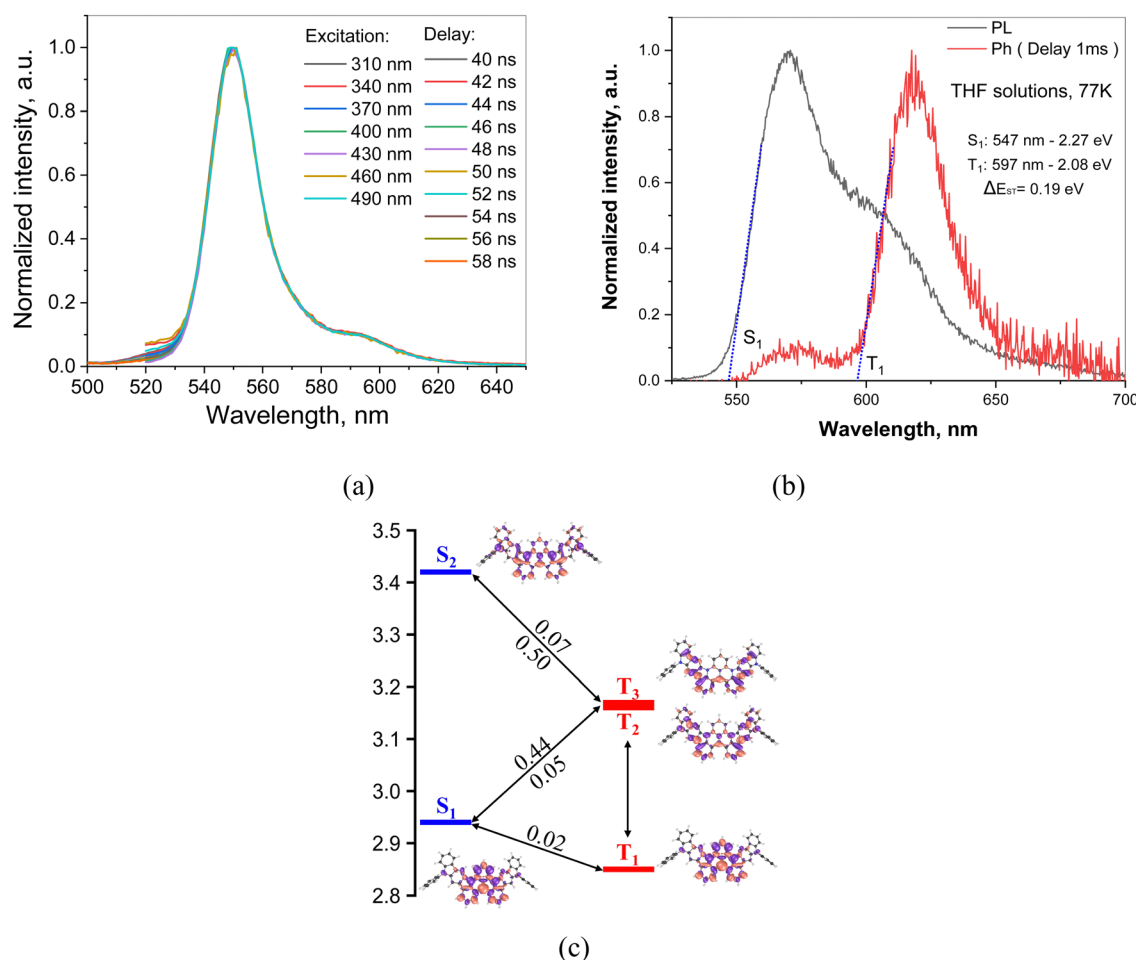

(a)

(b)

(c)

Fig. 4 (a) PL spectra at different excitation and delay times after excitation of **DG7** in toluene (10^{-6} M). The PL spectra were plotted from PL decay curves of time-resolved emission spectra (TRES). (b) Fluorescence and phosphorescence spectra of **DG7** in THF solution at 77 K (λ_{ex} = 330 nm). (c) SCS-CC2/cc-PVDZ energy diagram for the low-lying singlet and triplet excited states. The density difference plots with respect to the ground state are also shown for each excited state. A selection of spin–orbit couplings (SOC) between singlet and triplet states is also shown. * In the figure are shown the results obtained at the wB97XD/6-311G(d,p) level.

This journal is © The Royal Society of Chemistry 2024

J. Mater. Chem. C, 2024, **12**, 3450–3464 | **3455**

Table 2 Photophysical parameters of **DG7** in different media

Media	Toluene (10^{-5} M^{-1}) at λ_{ex} 530/350^d nm	THF (10^{-5} M^{-1}) at 296/77 K	Zeonex (1 wt%)	mCP (5/8 wt%)	TPBi (5/8 wt)	Neat film
λ^{PL},^{a} nm	552	569/570	550	564/563	567/566	568
FWHM,^{b} nm	20	51/50	30	34/34	55/34	30
PLQY,^{cf} %	100 (57^e)/96 (46^e)	—	68	19/12	13/11	4

^{a} Wavelength of the peak of PL spectrum. ^{b} Full-width at half-maximum. ^{c} Photoluminescence quantum yield determined using an integrating sphere. ^{d} Excitation wavelength. ^{e} Values obtained for air-containing toluene solution of **DG7**. ^{f} Obtained in air, recalculated for vacuum.

air-equilibrated and degassed dilute toluene solution of **DG7** exhibits the same decent yellowish-green emission with an emission peak maximum λ^{PL} at 552 nm and a FWHM of 20 nm (0.09 eV) (Fig. S5, ESI†). Using the integrating sphere, PLQY values of diluted toluene solution of **DG7** were measured (Table 2), approaching 100% in the degassed/sonicated toluene solution. When air is present in the dilute toluene solution, the emission intensity of **DG7** decreases and the PLQY is reduced to 57%. Because the excitation wavelength of 530 nm is not enough to populate states above S_1, and that the S_1 radiative decay rate is high and the ISC $S_1 \rightarrow T_1$ is practically El Sayed forbidden, we conclude that the triplets in this case are absent, and that both the sonication and N_2 bubbling only help eliminate PL quenching of singlet states by destroying the remaining micro-aggregates of **DG7**. In the case of an excitation wavelength of 350 nm, only slightly lower PLQY values of 96 and 46% were obtained for the degassed/sonicated and air-containing toluene solutions, respectively (Table 2). Given the similarly important impacts of the sonication on the emission intensities shown in Fig. 3e and f, and the potentially similar type of effects that bubbling the toluene solution with N_2 could have on the emission intensity, we conclude that the impact of oxygen on the triplet excitons as shown in Fig. 3e (excitation at 350 nm) is also very small (see Annex I, ESI†).

The absence of contribution from the triplet excitons in the PL emission spectra in toluene solutions is intriguing. Additionally, the experimental results indicate absence of delayed FL in toluene solutions or in the solid film, despite the relatively small $\Delta E(S_1-T_1)$ (0.08–0.09 eV and 0.19 eV obtained theoretically and experimentally, respectively), see Fig. 4b. This characteristic of **DG7** is similar to those of other MR-TADF compounds with missing TADF behavior in their dilute solutions, and can be explained by (i) the fast radiative decay timescale of the S_1 state and (ii) the very small SOC of 0.02 cm^{-1} that is found between S_1 and T_1 (Fig. 4c), in turn being easily explained in the frame of El Sayed's rule:[55] S_1 and T_1 have very similar nature, as can be seen from the density difference plots, see Fig. 4d, making the spin–flip between them practically forbidden. However, while the very small S_1-T_1 SOC value of 0.02 cm^{-1} can explain the PL characteristics when the excitation energy is 530 nm, questions remain about the PL characteristics observed through excitation at 350 nm.

Crossing the information extracted so far from Fig. 3a, e, f and Fig. S6 (ESI†), it can be easily concluded that the excitation energy of 3.55 eV (350 nm) allows populating very probably the closely lying excited states S_2–S_4 of **DG7** in toluene solution

(Fig. 3a and Fig. S5, ESI†), as compared to the population of only S_1 when the excitation energy is 2.34 eV (530 nm, Fig. S8, ESI†) (cf. ESI,† Annex I). The diagram shown in Fig. 5c finally allows proposing a mechanism explaining the absence of delayed emission whatever the excitation wavelength (Fig. 4a): if S_2 is populated, the dominant part of the excitons relax to S_1 and then to S_0, but a small part of them might undergo ISC from S_2 to T_2 or S_1 to $T_{2/3}$. However, a PLQY of 100% in toluene when excited at 530 nm, and the absence of delayed emission in toluene solution whatever the excitation energy support the hypothesis that the different ISC channels to the triplet manifold of excited states and/or the IC within it are inefficient for **DG7** in toluene. This mechanism is expected to quench excitons by populating T_1 behaving as a dead-end for the singlet and triplet excitons, which subsequently deexcite non-radiatively to the ground state. Indirect support to this mechanism seems to come from the presence of a weak DF band for **DG7** in THF at 77K (Fig. 4b): we hypothesize this DF band stemming from a less endothermic (or possibly exothermic) S_1–$T_{2/3}$ energy gap in THF as compared to toluene, due to the presence of larger CT character for $T_{2/3}$ as compared to T_1 (Fig. 2a), which would increase the S_1–$T_{2/3}$ spin orbit coupling.

Solid mixtures. To gain more insights into the presence or absence of DF, temperature-dependent steady-state and time-resolved emission measurements were performed for the Zeonex and **DG7** solid mixture (1%). Fig. 5a shows normalized PL spectra of the films of **DG7** recorded at different temperatures. Unlike the dilute toluene solution, significantly longer fluorescence lifetimes were recorded for the Zeonex and **DG7** solid mixture. The PL decay curves of the Zeonex and **DG7** solid mixture exhibited double exponential decays containing both PF in the nanosecond scale and delayed fluorescence (DF) components in the millisecond region. Temperature-dependence of the delayed lifetime was observed for the **DG7** MR-TADF emitter, and the intensity of DF was found to increase with the increase of the temperature between 77 and 300 K (Fig. 5b), thus confirming the TADF behavior.[52]

The observation of DF in the Zeonex and **DG7** solid mixture is intriguing, given that Zeonex is an inert non-emissive polymer and hence, no exciplex formation is expected between **DG7** and Zeonex that could lead to DF.[56] We hypothesize that the solid state polarization and/or distribution of geometrical configurations of **DG7** in Zeonex might impact the S_1, T_1 and/or T_2 energies, given their different space localizations in the central part and on the indolocarbazole arms, respectively (see Fig. 2c). Note that the distribution of geometrical configurations

3456 | *J. Mater. Chem. C*, 2024, **12**, 3450–3464

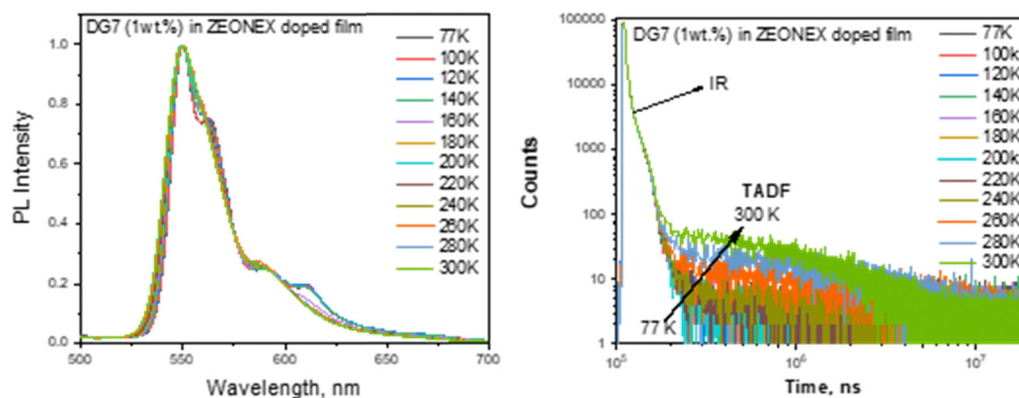This journal is © The Royal Society of Chemistry 2024

Fig. 5 Normalized PL spectra (a) and PL decay curves (b) of the Zeonex doped film of **DG7** (1 wt%) recorded at different temperatures.

considered here comes from a static distribution of the most flexible molecular degrees of freedom (dihedral angles, bending of the **DG7** core) leading to a further enhancement of the (non-)planarity of **DG7** generally arising in the amorphous solid state, which impacts directly the energy gaps between the different excited states while the dynamic configurational disorder in solution associated with molecular vibrations leaves these gaps unchanged. The geometrical aspect is discussed in Annex II (ESI†) based on the results from molecular dynamics simulations followed by DFT calculations. The results suggest that some geometrical deformations in **DG7** induced by the molecular dynamics simulations help in changing the energy gaps between the excited states but it occurs only in few instances (T_1–T_2 is taken as an example in Fig. S9, ESI†). In addition, because of the weak dielectric constant of Zeonex, it is unlikely that the excited energy gaps would be modulated by solid state polarization effects. A last hypothesis to rationalize the presence of a delayed fluorescence could arise from the damping/reduction of the amplitude of vibrational modes associated with non-radiative decay channels. In the end the large energy gaps between S_1, T_1 and T_2 (Fig. 4c) seem consistent with the DF duration in the millisecond range, which is typically regarded as weak.

Neat films and guest–host mixtures of (8 wt%) **DG7** with mCP, mCBP, and with TPBi hosts were additionally characterized theoretically and/or experimentally, see Fig. 6a–e. Recorded spectra in different hosts exhibit intense green fluorescence with sharp emission peaks at 563, 566 and 568 and small full-width at half-maxima (FWHMs) of 34, 34 and 30 nm, in mCP and in TPBi hosts, and in neat film, respectively (Table 2). Fig. 6a exhibits a small shoulder around 625 nm of increasing intensity with increasing temperature; however the relative intensity of this shoulder as compared to the main peak and the temperature impact on its intensity are very small. Importantly, the solid-state PLQY values for mCP- and TPBi-doped samples of 5 wt% **DG7** and its neat film were only 19, 13, and 4%, respectively, and were reduced to 12 and 11%, respectively for the 8 wt% **DG7**–host mixtures (Table 2 and Fig. S10–S13, ESI†). These results indicate that both **DG7**–mCP and **DG7**–TPBi mixtures and the neat film of **DG7** show very weak delayed fluorescence and TADF efficiencies, which are very

different from those reported for other MR-TADF compounds, like DABNA-1, which was attributed to a strong exciplex emission when mixed with mCBP[53].

In order to better understand the impact of the **DG7**–host interactions on the observed DF, from the MD simulation described in Annex II (ESI†) we extracted the molecular configurations of the closest contact between **DG7** and the host molecules, and subsequently performed hh-tda/b3lyp/def2-svp calculations on them. While the results shown in Fig. 6c and Fig. S14 (ESI†) indeed indicate examples of **DG7**–host associations, the very small host contribution (% of LUMO-host in the optical transition) allows excluding the presence of exciplexes. Similar comments apply for the **DG7**–mCP mixture. Additionally, the **DG7**–host energy diagrams shown in Fig. 6d and e suggest possible Dexter energy transfer from **DG7** to mCP.

Interestingly, the DF lifetime is practically the same for the three solid mixtures of **DG7** with Zeonex, mCP, and DPEPO (1.3–1.4 ms), suggesting similar nature for the DF in the three systems. Given the absence of exciplex formation in Zeonex, and the similar conclusion deduced from the results of our MD followed by hh-TDA calculations on **DG7**–host mixtures (Fig. 6c and Fig. S14, ESI†), we conclude that the main source for the (weak) DF in the case of mCP and DPEPO is not from exciplex formation but from some geometrical configurations exhibiting some intramolecular changes inducing a change in the guest electronic structure (i.e. energy gap between excited states), stemming from different guest–host interactions. Furthermore, the overall impact of **DG7** geometrical distortions on the DF efficiency is expected to be small, as confirmed by the theoretical results shown in Fig. S9e and f (ESI†), indicating that the majority of the molecular conformations correspond to large energy gaps between excited states.

We close this section by suggesting two main effects explaining the huge difference between the solution and the solid state PLQY: (i) presence of **DG7** microaggregates in **DG7**–host and **DG7**–Zeonex mixtures, resulting in important exciton quenching much larger for the **DG7**–host because of the higher concentration in **DG7**. This finds support from the strong sonication and bubbling effects observed in toluene solution, and from the smaller PLQY found in **DG7**–host mixtures with
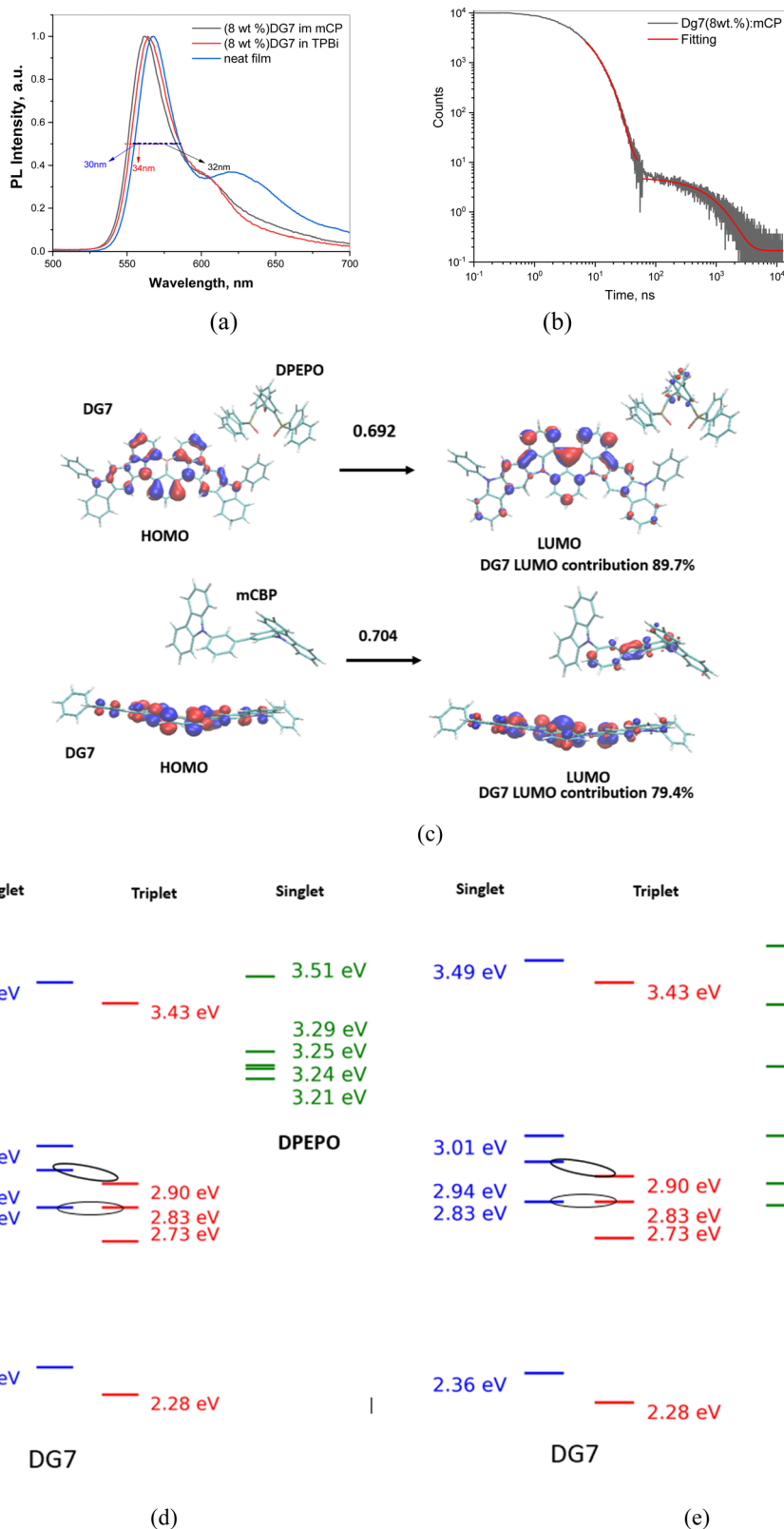
This journal is © The Royal Society of Chemistry 2024

J. Mater. Chem. C, 2024, **12**, 3450–3464 | **3457**

(a)

(b)

(c)

(d)

(e)

Fig. 6 (a) Normalized PL spectra of the DPEPO, mCP, and TPBi doped film of **DG7** (λ_{exc} = 330 nm). (b) PL decay curve of the mCP doped film of **DG7** (λ_{exc} = 330 nm). (c) Example of **DG7**–DPEPO and **DG7**–mCBP complexes extracted from molecular dynamics simulations. The MO contributions to the first excited state (S_1) are also shown, indicating formation of an exciplex with a weak contribution from DPEPO or mCBP. (d) and (e) Comparative energy diagrams between **DG7** (Hh-tda/b3lyp/def-2svp −0.45 eV to be in line with experiment) and DPEPO (d) and mCB (e) as reported previously[57].

3458 | *J. Mater. Chem. C*, 2024, **12**, 3450–3464

This journal is © The Royal Society of Chemistry 2024

8 wt% as compared to 5 wt% (Table 2). (ii) Singlet and triplet quenching by oxygen, as supported by the important intensity differences from measurements in air and in degassed and sonicated toluene solutions.

Electroluminescence. Promised by the narrowband emission of compound **DG7**, its electroluminescent properties were investigated by fabricating devices with the following architecture of indium tin oxide (ITO)/molybdenum trioxide (MoO$_3$, 2 nm)/tris(4-carbazolyl-9-ylphenyl)amine (TCTA, 64 nm)/emitting layer (10 nm)/2,2′,2″-(1,3,5-benzinetriyl)-tris(1-phenyl-1-*H*-benzimidazole) (TPBi, 10 nm)/4,7-diphenyl-1,10-phenanthroline doped by cesium (BPhen: Cs, 50 nm)/aluminum (Al, 100 nm) (Fig. S15a, ESI†). We used a similar OLED stack to that previously reported by Meyer *et al.*[46] Herein, ITO and Al were the anode and the cathode, respectively. MoO$_3$ served as the hole-injection layer, TCTA functioned as the hole-transporting layer and electron blocking layer, TPBi was applied mostly as hole-blocking layer and BPhen:Cs served as the electron-transporting and electron-injection layer. Regarding the emissive layers, TPBi and 1,3-bis(*N*-carbazolyl)-benzene (mCP) were selected as the host materials. The effects of different host materials on the electroluminescence efficiency of

DG7 were investigated. To evaluate the EL performance of **DG7** more precisely and by varying the evaporation rate of **DG7**, OLEDs with different guest concentrations of 5 and 8 wt% were fabricated. Thus, we investigated four devices (named devices 1–4) with emission layers (EMLs) of **DG7**(5 wt%):TPBi, **DG7**(8 wt%):TPBi, **DG7**(5 wt%):mCP, and **DG7**(8 wt%):mCP, respectively. The equilibrium energy-level diagram and molecular structures of the functional materials are depicted in Fig. 7.

The efficient injection of charge carriers from ITO and aluminum electrodes and the following transport to emissive layers of all the fabricated OLEDs are confirmed by their low turn-on voltages (3.1–3.6 V at a luminance of 1 cd m^{-1}) (Fig. 8a and Table 3). With the decreased concentration of **DG7** in the hosts from 8 to 5 wt%, devices 1 and 3 showed higher efficiency than devices 2 and 4, respectively (Fig. 8b and Table 3). The highest maximum brightness of 9176 cd m^{-2} at 10 V, the maximum power efficiency of 7 lm W^{-1} and the maximum external quantum efficiency of 2.8% were observed for device 3 with 5% of **DG7** dispersed in the mCP host as the emitting layer. Devices 1–4 showed low EQE and drastic efficiency roll-off.
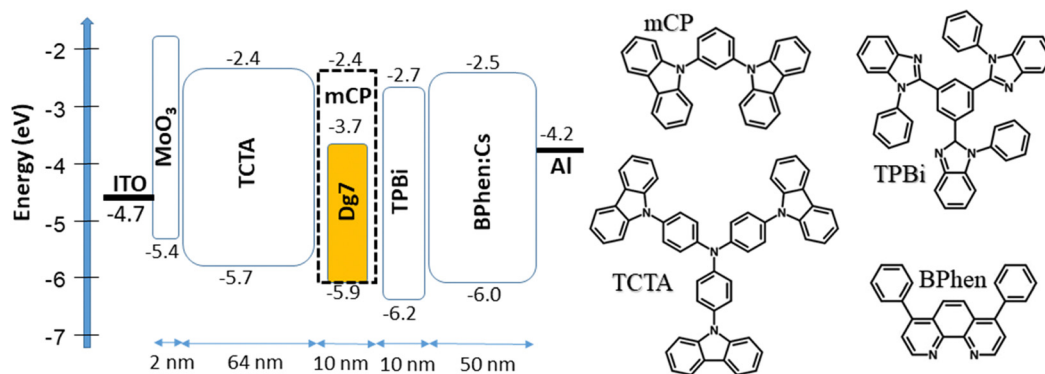

Fig. 7 Visualized device structures representing the equilibrium energy diagram and molecular structures of the compounds used in the OLEDs.
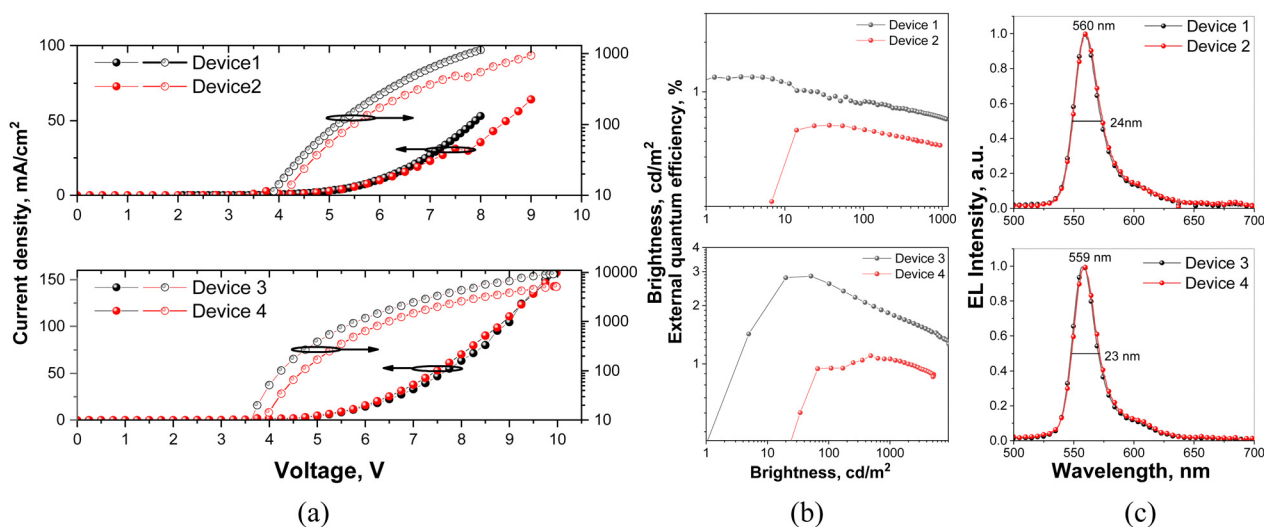

Fig. 8 Normalized EL spectra (a), current density/brightness *versus* applied voltage (b), and external quantum efficiency (c) *versus* brightness.

This journal is © The Royal Society of Chemistry 2024

J. Mater. Chem. C, 2024, **12**, 3450–3464 | **3459**

Table 3 Parameters of OLEDs

Device	EML	$V_{on},^a$ V	Max brightness,^{b} cd m^{-2}	PE$_{1000}$/EQE$_{1000}$^{c} (lm W^{-1}/%)	PE$_{max}$/EQE$_{max}$^{d} (lm W^{-1}/%)	$\lambda,^e$ nm	CIE, x,y	FWHM, nm
OLED structures: ITO/MoO$_3$/TCTA/EML/TPBi/BPhen:Cs/Al								
1	**DG7**(5 wt%):TPBi	3.1	1128	0.7/0.7	2.7/1.2	560	0.42, 0.54	24
2	**DG7**(8 wt%):TPBi	3.6	941	—/—	1.1/0.6	560	0.43, 0.54	24
3	**DG7**(5 wt%):mCP	3.3	9176	2.9/1.8	7/2.8	559	0.41, 0.55	23
4	**DG7**(8 wt%):mCP	3.5	5079	1.1/1	2.5/1.1	559	0.41, 0.54	23

^{a} Turn-on voltage at a luminance of 1 cd m^{-1}. ^{b} Maximum brightness. ^{c} Power efficiency and external quantum efficiency at 1000 cd m^{-2}. ^{d} Maximum power efficiency, and maximum external quantum efficiency. ^{e} Maxima of EL (λ_{max}) spectra.

These efficiencies and their trends are coherent with the weak TADF efficiency and small PLQY values of the light-emitting solid layers (Fig. S10–S13, ESI† and Table 2). Thus, severe intermolecular aggregation and exciton loss channels of compound **DG7** dispersed in different hosts result in strong ACQ of **DG7** emission and the absence of efficient triplet harvesting, which constitute the main reasons for the relatively low maximum EQE value of 2.8% of **DG7**-based OLEDs.

In spite of these drawbacks, **DG7** demonstrated high color purity of electroluminescence (EL). The EL performances of the OLEDs are shown in Fig. 8c and relevant parameters are summarized in Table 3. The shapes of EL spectra of the fabricated OLEDs were in good agreement with the PL profiles. They showed yellowish green emission with peaks at 560 and 559 nm as well as narrow FWHM values of 24 and 23 for devices based on TPBi and mCP hosts, respectively (Fig. 8c and Table 3). The CIE color coordinates of the **DG7** devices are collected in Table 3 and shown in Fig. S15b (ESI†). The emission peaks and FHWM values show no change with the increase of doping concentration from 5 wt% to 8 wt%.

Discussion

The indolocarbazole-based MR-TADF emitter presents a unique scenario: while it exhibits outstanding optical properties in solution, reaching a PLQY of 100% in degassed and sonicated toluene, the PLQY in solid mixtures or neat film is reduced to less than 12%, and its EQE of only 2.8% in OLEDs is subpar. Still, these results are quite coherent if one combines the moderate PLQY values of 12–19% in host:guest systems also used in the OLEDs (*cf.* Table 2) with a typical value of 20% for the outcoupling efficiency, by additionally assuming 100% of singlet–triplet harvesting and 100% of charge balance. The main limitation to higher EQE seems to be the low PLQY of **DG7** in the corresponding thin films. Accordingly, there is a first-sight dichotomy between the efficient singlet–triplet harvesting deduced from the electroluminescence measurement in the devices, and the absence of DF deduced from the photoluminescence measurements in toluene solutions. However, the DF timescale of several ms indicates the presence of long-living triplet species, which, in the devices, are expected to take advantage from different slow- or fast channels to undergo rISC. Amongst possible triplet-to-singlet rISC channels present in the devices regardless of their (in)efficiency, the direct S$_1$–T$_1$

channel or a mechanism which would involve higher-lying triplet states such as T$_2$ and T$_3$ could not be excluded in view of the associated energy gaps in the guest–host mixtures. The decrease of the EQE with increased brightness could be associated with annihilation processes such as triplet–triplet annihilation or triplet–polaron annihilation.

Accordingly, this huge discrepancy between the toluene solution and the solid-state results seems to stem from a joint contribution from different factors: (i) because of the rigid molecular planar structure, **DG7** is prone to strong π–π stacking interactions, leading to the presence of microaggregates even in solution, with a direct impact on ACQ. (ii) The above effect is strongly enhanced in the presence of oxygen. Our study suggests additional significant effects on singlet quenching that could be prevalent in MR-TADF, in addition to common triplet quenching by oxygen. (iii) The energy gaps between the different relevant excited states S$_1$, T$_1$ and T$_{2/3}$ which limit the DF. The excited state ordering could also be responsible for the very slow device operation.

Consequently, avoiding both aggregation and design of compounds with a small T$_1$–T$_2$ energy gap is crucial for reaching excellent performances with the MR-TADF compounds in general. While the aggregation effect can be overcome by inducing steric hindrance, avoiding a large T$_1$–T$_2$ energy gap is more challenging. Aiming at obtaining insights into the latter parameter, in Fig. 9 we consider five MR-TADF molecules, including two real molecules, **DG7** and DABNA-1, along with three model compounds named Model-1 to Model-3. In Fig. 9a we present the HOMO, HOMO−1, and HOMO−2 pictograms of the five molecules and their ΔE(T$_1$–T$_2$) and ΔE(T$_2$–T$_3$) values, whereas in Fig. 9b we show the correlation between ΔE(T$_1$–T$_2$) and ΔE(T$_2$–T$_3$) with ΔE(H–H$_{-1}$) and ΔE(H$_{-1}$–H$_{-2}$), respectively. Based on the good correlations shown in Fig. 9b, in the following we follow the evolution of ΔE(T$_1$–T$_2$) for the five molecules based on the characteristics of their three highest occupied MOs.

First, we consider **DG7**. Fig. 2b and Table S1 (ESI†) indicate that T$_1$ corresponds to the HOMO → LUMO transition, both of MOs being localized in the central part of **DG7**, whereas T$_2$ seems to involve transitions from HOMO−2 localized on the lateral indolocarbazole fragments. Accordingly, the electronic density-differences between ground- and excited states for T$_1$ and for T$_2$ are distributed in different molecular moieties of **DG7**, in the central part for T$_1$ and in the indolocarbazole arms for T$_2$ (Fig. 9a). These moieties are of a very different nature, thus giving rise to very different triplet energies.

3460 | *J. Mater. Chem. C*, 2024, **12**, 3450–3464
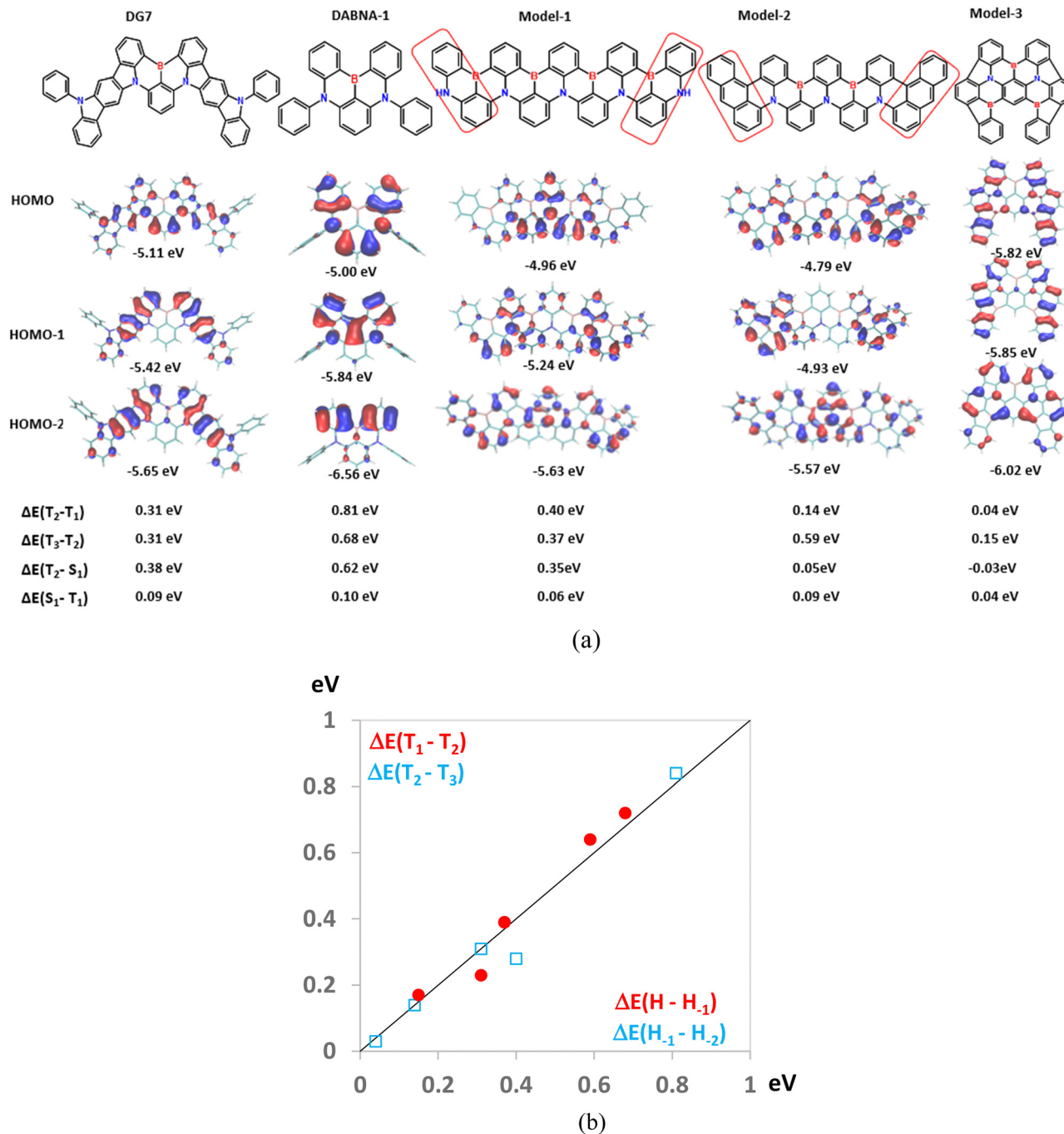
This journal is © The Royal Society of Chemistry 2024

Fig. 9 (a) HOMO−2, HOMO−1, and HOMO of the indicated molecules, along with $\Delta E(T_1-T_2)$ and $\Delta E(T_2-T_3)$. (b) Correlation between $\Delta E(T_1-T_2)$ and $\Delta E(T_2-T_3)$ with the energy differences between the HOMO and HOMO−1, reported as $\Delta E(H-H_{-1})$, and between HOMO−1 and HOMO−2, reported as $\Delta E(H_{-1}-H_{-2})$, respectively.

Note that HOMO−1 and HOMO−2 of **DG7** correspond to the out-of-phase and in-phase combinations of the two local-indolocarbazole HOMOs (Fig. 9a), with the corresponding energies being obviously lower than the energy of the central-core fragment of **DG7**. It is tempting to think that, in a new **DG7**-like molecule, the $\Delta E(T_1-T_2)$ could be much smaller if the constitution of the lateral fragments were to be such that HOMO-**DG7** (localized on the molecular central core) becomes

HOMO−2 in a new **DG7**-like molecule. We assume consequently that one possible way to tune $\Delta E(T_1-T_2)$ would be to tune $\Delta E(H-H_{-1})$ by making these MOs delocalized on identical fragments.

To this aim, and for the sake of simplicity, we focus on the B,N containing MR-TADF compounds. Most of them contain a central pseudo-symmetry plane (or axes) orthogonal to (lying on) the average molecular plane; however, the conclusions

This journal is © The Royal Society of Chemistry 2024

J. Mater. Chem. C, 2024, **12**, 3450–3464 | **3461**

drawn below hold true independently of the molecular shape. From the chemical-composition standpoint, these molecules either contain a homogenous and symmetrical MR π-conjugated system like DABNA-1 or Model-1, or (ii) like in **DG7**, they contain a homogenous symmetrical MR-TADF central core, and two identical lateral fragments generally fused to the MR-TADF core.

First, we highlight that designing MR-TADF compounds exhibiting total chemical homogeneity with respect to the central pseudo-symmetry plane seems to be not a good idea. Indeed, the in-phase combination of the two ''half-HOMOs'' (the local-HOMOs of the two left- and right molecular halves) is expected to strongly overlap between them, thus resulting in large $\Delta E(\text{H–H}_{-1})$ and $\Delta E(\text{T}_1\text{–T}_2)$. This factor is, for instance, the reason why DABNA-1 exhibits huge $\Delta E(\text{T}_1\text{–T}_2)$ of 0.8 eV (Fig. 9a). Increasing the space delocalization of the π-conjugated system by enlarging the molecular size and keeping the homogeneous chemical constitution as in the case of Model-1 (Fig. 9a) is indeed helpful in reducing the overlap between the two half-HOMOs but cannot prevent them from strongly overlapping in the center of the molecule, in addition to the increased propensity for aggregation. The HOMO of Model-1 is indeed strongly localized in the center of the molecule, whereas HOMO−1 is localized on the lateral parts of the molecule, thus resulting in a very high $\Delta E(\text{T}_1\text{–T}_2)$ of 0.4 eV.

It is then clear that avoiding strong energy splitting between the HOMO and HOMO−1 would need designing molecules containing lateral groups of different chemical constitution as compared to the central part. Indeed, replacing the lateral parts of Model-1 by anthracene-like groups like in Model-2 is found to localize the half-HOMOs on the lateral parts and reduce their overlap in the central part, thus resulting in strongly reduced $\Delta E(\text{H–H}_{-1})$ and in $\Delta E(\text{T}_1\text{–T}_2)$ of only 0.14 eV.

Finally, in Fig. 9a we show another model molecule, named Model-3, with similar size to **DG7**, but exhibiting the desired order between the three lowest occupied MOs: HOMO−2 is localized in the central core, and HOMO−1 and HOMO are localized on the lateral fragments. This result indicates a larger donor character for the lateral fragments of Model-3 as compared to the central core. Accordingly, small $\Delta E(\text{T}_1\text{–T}_2)$ and $\Delta E(\text{T}_2\text{–T}_3)$ values of 0.04 eV and 0.15 eV were found, respectively. Consequently, the comparison between Model-2 and Model-3 on the one hand, and that between **DG7** and DABNA-1 on the other hand support the validity of the idea that $\Delta E(\text{T}_1\text{–T}_2)$ in MR-TADF compounds can be tuned by judiciously designing lateral groups of higher donor character as compared to the core, whereas the comparison between Model-2 and Model-3 indicates that increasing the size of the molecules is not mandatory for tuning $\Delta E(\text{T}_1\text{–T}_2)$. Interestingly, this design strategy results in a denser density of triplet states which has been proven to be beneficial for increasing the rate of RISC.[58] We speculate that such improved MR-TADF molecules would be able to exhibit intramolecular TADF behavior as opposed to the absence of this desired property for most of the previously reported MR-TADF compounds.

Conclusions

The synthesis, characterization, and comprehensive study of a boron-based MR-TADF compound have demonstrated the intricate relationship between the molecular structure, aggregation, and photophysical properties. **DG7** toluene solution exhibits outstanding optical properties, reaching a photoluminescence quantum yield of 100% for the degassed and sonicated sample, and an ultra-pure green-yellow emission with a full width at half maximum (FWHM) of only 20 nm. Despite the high solution PLQY, **DG7** experienced a dramatic reduction of PLQY of the solid mixtures. This was attributed to strong π–π stacking interactions, in turn stemming from the rigid planar molecular structure, leading to aggregation-induced quenching. Like other MR-TADF compounds, **DG7** exhibits no delayed fluorescence in toluene solution, which is attributed to the large energy gap between the two lowest triplet excited states. Our theoretical analysis on this behavior points to some fundamental aspects in correlation with the chemical constitution. The insights gained from **DG7** suggest that optimization of MR-TADF compounds requires a careful balance between molecular design to prevent aggregation and strategic engineering of energy gaps to enhance TADF efficiency.

Based on our results, one possible design strategy for new efficient MR-TADF emitters would need (i) avoiding the tendency for aggregation by inducing steric hindrance at some peripheral ''strategic'' positions, and (ii) combining lateral groups of higher donor character (higher local-HOMO) as compared to the molecular central core, which can be reached by a judicious combination of size and/or chemical constitution of lateral moieties.

Author contributions

Conceptualization – Rasa Keruckiene, Dmytro Volyniuk, Gjergji Sini; methodology and investigation – Aliaksei A. Vaitusionak, Maksim I. Hulnik, Ivan A. Berezianko, Dalius Gudeika, Simas Macionis, Malek Mahmoudi; validation and data curation – Danillo Valverde, Yoann Olivier Kai Lin Woon, Sergei V Kostjuk, Sebastian Reineke; formal analysis and writing – original draft – Yoann Olivier, Kai Lin Woon, Sebastian Reineke, Gjergji Sini; writing – review and editing – Yoann Olivier, Gjergji Sini; supervision and funding acquisition – Juozas. V. Grazulevicius.

Conflicts of interest

The authors declare that there is no conflict of interest regarding the publication of this paper.

Acknowledgements

3462 | *J. Mater. Chem. C*, 2024, **12**, 3450–3464

This journal is © The Royal Society of Chemistry 2024

References

1 K.-L. Woon, C.-L. Yi, K.-C. Pan, M. K. Etherington, C.-C. Wu, K.-T. Wong and A. P. Monkman, *J. Phys. Chem. C*, 2019, **123**, 12400–12410.

2 L. Skhirtladze, K. Lietonas, A. Bucinskas, D. Volyniuk, M. Mahmoudi, O. Mukbaniani, K. L. Woon, A. Ariffin and J. V. Grazulevicius, *J. Mater. Chem. C*, 2022, **10**, 4929–4940.

3 W. Derkowski, D. Kumar, T. Gryber, J. Wagner, M. Morawiak, M. A. Kochman, A. Kubas, P. Data and M. Lindner, *Chem. Commun.*, 2023, **59**, 2815–2818.

4 F. Baraket, B. Pedras, É. Torres, M. J. Brites, M. Dammak and M. N. Berberan-Santos, *Dyes Pigm.*, 2020, **175**, 108114.

5 L. Gan, Z. Xu, Z. Wang, B. Li, W. Li, X. Cai, K. Liu, Q. Liang and S. Su, *Adv. Funct. Mater.*, 2019, **29**, 1808088.

6 Y. Im, M. Kim, Y. J. Cho, J.-A. Seo, K. S. Yook and J. Y. Lee, *Chem. Mater.*, 2017, **29**, 1946–1963.

7 P. Stachelek, J. S. Ward, P. L. dos Santos, A. Danos, M. Colella, N. Haase, S. J. Raynes, A. S. Batsanov, M. R. Bryce and A. P. Monkman, *ACS Appl. Mater. Interfaces*, 2019, **11**, 27125–27133.

8 J. Wang, Y. Yang, P. Xu, Z. Cang, C. Yao and X. Zhai, *J. Lumin.*, 2023, **263**, 120087.

9 J. Wang, X. Zhai, C. Ji, M. Zhang, C. Yao, G. Xie, J. Zhang and X. Xi, *Dyes Pigm.*, 2023, **219**, 111586.

10 J. Wang, Y. Yang, C. Jiang, M. He, C. Yao and J. Zhang, *J. Mater. Chem. C*, 2022, **10**, 3163–3171.

11 J. Wang, J. Zhang, C. Jiang, C. Yao and X. Xi, *ACS Appl. Mater. Interfaces*, 2021, **13**, 57713–57724.

12 J. Li, R. Zhang, Z. Wang, B. Zhao, J. Xie, F. Zhang, H. Wang and K. Guo, *Adv. Opt. Mater.*, 2018, **6**, 1701256.

13 X. Liu, Y.-F. Wang, M. Li, Y. Zhu and C.-F. Chen, *Org. Electron.*, 2021, **88**, 106017.

14 H. Xie, Z. Huang, N. Li, T. Hua, J. Miao and C. Yang, *J. Mater. Chem. C*, 2022, **10**, 11239–11245.

15 J. Gibson, A. P. Monkman and T. J. Penfold, *ChemPhysChem*, 2016, **17**, 2956–2961.

16 M. K. Etherington, J. Gibson, H. F. Higginbotham, T. J. Penfold and A. P. Monkman, *Nat. Commun.*, 2016, **7**, 13680.

17 T. Serevičius, R. Skaisgiris, J. Dodonova, L. Jagintavičius, J. Bucevičius, K. Kazlauskas, S. Juršėnas and S. Tumkevičius, *Chem. Commun.*, 2019, **55**, 1975–1978.

18 T. Serevičius, R. Skaisgiris, J. Dodonova, K. Kazlauskas, S. Juršėnas and S. Tumkevičius, *Phys. Chem. Chem. Phys.*, 2020, **22**, 265–272.

19 M. Mahmoudi, D. Gudeika, S. Kutsiy, J. Simokaitiene, R. Butkute, L. Skhirtladze, K. L. Woon, D. Volyniuk and J. V. Grazulevicius, *ACS Appl. Mater. Interfaces*, 2022, **14**, 40158–40172.

20 T. Hatakeyama, K. Shiren, K. Nakajima, S. Nomura, S. Nakatsuka, K. Kinoshita, J. Ni, Y. Ono and T. Ikuta, *Adv. Mater.*, 2016, **28**, 2777–2781.

21 Y. Cheng, X. Fan, F. Huang, X. Xiong, J. Yu, K. Wang, C. Lee and X. Zhang, *Angew. Chem., Int. Ed.*, 2022, **61**, e202212575, DOI: **10.1002/anie.202212575**.

22 S. Madayanad Suresh, L. Zhang, D. Hall, C. Si, G. Ricci, T. Matulaitis, A. M. Z. Slawin, S. Warriner, Y. Olivier, I. D. W. Samuel and E. Zysman-Colman, *Angew. Chem., Int. Ed.*, 2023, **62**, e202215522, DOI: **10.1002/anie.202215522**.

23 W. Yang, J. Miao, F. Hu, Y. Zou, C. Zhong, S. Gong and C. Yang, *Adv. Funct. Mater.*, 2023, 2213056.

24 K. R. Naveen, H. I. Yang and J. H. Kwon, *Commun. Chem.*, 2022, **5**, 149.

25 T. Hatakeyama, K. Shiren, K. Nakajima, S. Nomura, S. Nakatsuka, K. Kinoshita, J. Ni, Y. Ono and T. Ikuta, *Adv. Mater.*, 2016, **28**, 2777–2781.

26 S. H. Han, J. H. Jeong, J. W. Yoo and J. Y. Lee, *J. Mater. Chem. C*, 2019, **7**, 3082–3089.

27 X. Liang, Z. P. Yan, H. B. Han, Z. G. Wu, Y. X. Zheng, H. Meng, J. L. Zuo and W. Huang, *Angew. Chem., Int. Ed.*, 2018, **57**, 11316–11320.

28 J. H. Kim, W. J. Chung, J. Kim and J. Y. Lee, *Mater. Today Energy*, 2021, **21**, 100792.

29 Y. Kondo, K. Yoshiura, S. Kitera, H. Nishi, S. Oda, H. Gotoh, Y. Sasada, M. Yanai and T. Hatakeyama, *Nat. Photonics*, 2019, **13**, 678–682.

30 Y. Zhang, D. Zhang, J. Wei, Z. Liu, Y. Lu and L. Duan, *Angew. Chem., Int. Ed.*, 2019, **58**, 16912–16917.

31 Y. Xu, Z. Cheng, Z. Li, B. Liang, J. Wang, J. Wei, Z. Zhang and Y. Wang, *Adv. Opt. Mater.*, 2020, **8**, 1902142.

32 F. Liu, Z. Cheng, L. Wan, Z. Feng, H. Liu, H. Jin, L. Gao, P. Lu and W. Yang, *Small*, 2022, **18**, 2106462.

33 X. Yan, Z. Li, Q. Wang, Y. Qu, Y. Xu and Y. Wang, *J. Mater. Chem. C*, 2022, **10**, 15408–15415.

34 M. Yang, I. S. Park and T. Yasuda, *J. Am. Chem. Soc.*, 2020, **142**, 19468–19472.

35 Y. Liu, X. Xiao, Y. Ran, Z. Bin and J. You, *Chem. Sci.*, 2021, **12**, 9408–9412, DOI: **10.1039/d1sc02042k**.

36 M. Yang, S. Shikita, H. Min, I. S. Park, H. Shibata, N. Amanokura and T. Yasuda, *Angew. Chem., Int. Ed.*, 2021, **60**, 23142–23147.

37 Y. Xu, C. Li, Z. Li, J. Wang, J. Xue, Q. Wang, X. Cai and Y. Wang, *CCS Chem.*, 2022, **4**, 2065–2079.

38 L. Lin, J. Fan, L. Cai and C.-K. Wang, *Mol. Phys.*, 2018, **116**, 19–28.

39 A. Pershin, D. Hall, V. Lemaur, J.-C. Sancho-Garcia, L. Muccioli, E. Zysman-Colman, D. Beljonne and Y. Olivier, *Nat. Commun.*, 2019, **10**, 597.

40 M. K. Etherington, J. Gibson, H. F. Higginbotham, T. J. Penfold and A. P. Monkman, *Nat. Commun.*, 2016, **7**, 13680.

41 J. Gibson, A. P. Monkman and T. J. Penfold, *ChemPhysChem*, 2016, **17**, 2956–2961.

42 T. J. Penfold, E. Gindensperger, C. Daniel and C. M. Marian, *Chem. Rev.*, 2018, **118**, 6975–7025.

This journal is © The Royal Society of Chemistry 2024

J. Mater. Chem. C, 2024, **12**, 3450–3464 | **3463**

43 T. J. Penfold, F. B. Dias and A. P. Monkman, *Chem. Commun.*, 2018, **54**, 3926–3935.

44 H. Tanaka, S. Oda, G. Ricci, H. Gotoh, K. Tabata, R. Kawasumi, D. Beljonne, Y. Olivier and T. Hatakeyama, *Angew. Chem., Int. Ed.*, 2021, **60**, 17910–17914.

45 S. Lee, H. Kim and Y. Kim, *InfoMat*, 2021, **3**, 61–81.

46 D. Hall, J. C. Sancho-García, A. Pershin, G. Ricci, D. Beljonne, E. Zysman-Colman and Y. Olivier, *J. Chem. Theory Comput.*, 2022, **18**, 4903–4918.

47 K. Stavrou, A. Danos, T. Hama, T. Hatakeyama and A. Monkman, *ACS Appl. Mater. Interfaces*, 2021, **13**, 8655.

48 Y. Xu, C. Li, Z. Li, J. Wang, J. Xue, Q. Wang, X. Cai and Y. Wang, *CCS Chem.*, 2022, **4**, 2065–2079.

49 G. Meng, L. Liu, Z. He, D. Hall, X. Wang, T. Peng, X. Yin, P. Chen, D. Beljonne, Y. Olivier, E. Zysman-Colman, N. Wang and S. Wang, *Chem. Sci.*, 2022, **13**, 1665–1674, DOI: **10.1039/d1sc05692a**.

50 Y. Y. Jing, Y. Yang, N. Li, Z. Ye, X. Wang, X. Cao and C. Yang, *Luminescence*, 2024, **1**, e4624, DOI: **10.1002/BIO.4624**.

51 N. Ikeda, S. Oda, R. Matsumoto, M. Yoshioka, D. Fukushima, K. Yoshiura, N. Yasuda, T. Hatakeyama, N. Ikeda, S. Oda, K. Yoshiura, T. Hatakeyama, R. Matsumoto, M. Yoshioka, D. Fukushima and N. Yasuda, *Adv. Mater.*, 2020, **32**, 2004072.

52 D. Hall, S. M. Suresh, P. L. dos Santos, E. Duda, S. Bagnich, A. Pershin, P. Rajamalli, D. B. Cordes, A. M. Z. Slawin, D. Beljonne, A. Köhler, I. D. W. Samuel, Y. Olivier and E. Zysman-Colman, *Adv. Opt. Mater.*, 2020, **8**, 1901627, DOI: **10.1002/ADOM.201901627**.

53 K. L. Woon, P. A. Nikishau and G. Sini, *Adv. Theory Simul.*, 2022, **5**, 2200056.

54 T. Hatakeyama, K. Shiren, K. Nakajima, S. Nomura, S. Nakatsuka, K. Kinoshita, J. Ni, Y. Ono and T. Ikuta, *Adv. Mater.*, 2016, **28**, 2777–2781.

55 B. Wu, H. Su, A. Cheng, X. Zhang, T. Wang and G. Zhang, *Cell Rep. Phys. Sci.*, 2023, **4**, 101245.

56 X. Wu, B.-K. Su, D.-G. Chen, D. Liu, C.-C. Wu, Z.-X. Huang, T.-C. Lin, C.-H. Wu, M. Zhu, E. Y. Li, W.-Y. Hung, W. Zhu and P.-T. Chou, *Nat. Photonics*, 2021, **15**, 780–786.

57 N. Notsuka, R. Kabe, K. Goushi and C. Adachi, *Adv. Funct. Mater.*, 2017, **27**, 1703902.

58 J. Eng, J. Hagon and T. J. Penfold, *J. Mater. Chem. C*, 2019, **7**, 12942–12952.

3464 | *J. Mater. Chem. C*, 2024, **12**, 3450–3464

This journal is © The Royal Society of Chemistry 2024